Check for updates

Low-concentration CO$_2$ capture using metal–organic frameworks – current status and future perspectives

Michelle Åhlén, Ocean Cheung [iD] * and Chao Xu [iD] *

The ever-increasing atmospheric CO$_2$ level is considered to be the major cause of climate change. Although the move away from fossil fuel-based energy generation to sustainable energy sources would significantly reduce the release of CO$_2$ into the atmosphere, it will most probably take time to be fully implemented on a global scale. On the other hand, capturing CO$_2$ from emission sources or directly from the atmosphere are robust approaches that can reduce the atmospheric CO$_2$ concentration in a relatively short time. Here, we provide a perspective on the recent development of metal–organic framework (MOF)-based solid sorbents that have been investigated for application in CO$_2$ capture from low-concentration (<10 000 ppm) CO$_2$ sources. We summarized the different sorbent engineering approaches adopted by researchers, both from the sorbent development and processing viewpoints. We also discuss the immediate challenges of using MOF-based CO$_2$ sorbents for low-concentration CO$_2$ capture. MOF-based materials, with tuneable pore properties and tailorable surface chemistry, and ease of handling, certainly deserve continued development into low-cost, efficient CO$_2$ sorbents for low-concentration CO$_2$ capture.

Introduction

The ever-increasing combustion of fossil fuels, such as energy generation in coal-fired power plants, cement plants, and oil refineries has contributed towards increasing the atmospheric CO$_2$ concentration.[1] The atmospheric CO$_2$ level has gone from the pre-industrial value of 280 ppm to a current level of 418 ppm (December 2022).[2] The greenhouse effect that is caused by the high atmospheric levels of CO$_2$ is considered to be one of the main reasons for global warming as well as the associated environmental issues. In addition to the irreversible changes to the climate and environment, a high atmospheric CO$_2$ concentration is a big risk to human health, for example, it can trigger respiratory illnesses when the atmospheric CO$_2$ concentration is over 600 ppm.[3] Although the move towards non-fossil fuel-based energy generation could be a long-term solution to reduce CO$_2$ emission due to human activities, carbon capture and storage (CCS) is undoubtedly an important current approach to reduce the CO$_2$ emission from point sources of CO$_2$. Alternatively, direct air capture (DAC) of CO$_2$, which implies not only capturing CO$_2$ from emission point sources, but rather from the atmosphere, is also an important complementary approach for reducing the atmospheric CO$_2$ level. DAC is a negative emission technology that has the potential to

lower the atmospheric CO$_2$ concentration down to 350 ppm.[4] DAC of CO$_2$ would mean capturing CO$_2$ from sources with low-concentrations, or trace amounts of CO$_2$. This type of CO$_2$ capture is important for gas purification, indoor air quality control, and a number of industrial processes. DAC of CO$_2$ has been discussed for indoor settings such as classrooms, hospitals, or offices in order to ensure the well-being of individuals. Air purification devices are needed in ventilators, or in confined spaces such as spacecraft and submarines to keep the CO$_2$ concentration at a safe level. From an industrial point of view, in order to meet the liquefied natural gas (LNG) specifications, CO$_2$ concentration in natural gas has to be reduced down to 50 ppm before its liquefaction.[5] These example application areas show that there is currently a great interest and urgent need for the development of efficient technology for low-concentration CO$_2$ capture. For the purpose of this perspective, we operationally define "low-concentration" as below approximately 10 000 ppm in CO$_2$ concentration.

Amine scrubbing is probably the most mature and viable CO$_2$ capture technology that has been widely applied in natural gas purification and post-combustion capture of CO$_2$.[6] It uses aqueous amine solutions to absorb CO$_2$ from gases *via* chemical reactions, which offers high separation and purification efficiencies even at ultralow CO$_2$ concentrations (<1000 ppm). However, amine scrubbing suffers from significant drawbacks such as high energy consumption for amine regeneration, risk of amine leakage, and corrosion to the associated equipment. Temperature or pressure swing adsorption (TSA, PSA) technologies have also been developed for CO$_2$

Division of Nanotechnology and Functional Materials, Department of Materials Science and Engineering, Uppsala University, Ångström Laboratory, SE-751 03 UppsalaBox 35, Sweden. E-mail: ocean.cheung@angstrom.uu.se, chao.xu@angstrom.uu.se; Tel: +46 18 471 3279, +46 18 471 3230

capture. These technologies can be adapted to utilize solid physisorbents. Physisorbents such as porous solids can be engineered to adsorb CO_2 selectively over other gases on the internal surfaces of the sorbent. The adsorbed CO_2 is then released at elevated temperatures and/or reduced pressures and the sorbent is regenerated for subsequent cycles.[7–9] In contrast to chemisorption processes (using chemisorbents), physisorbents adsorb CO_2 with relatively low enthalpy of adsorption (ΔH_{ads}). The energy cost for regeneration of physisorbents is much lower than for chemisorbents (where chemical bonds form between the sorbent and CO_2). Porous physisorbents including activated carbons,[10–12] zeolites,[13–16] silica,[17,18] and porous organic polymers[19–21] have been intensively studied for CO_2 capture. Some of these sorbents show great potential for post-combustion carbon capture, where CO_2 partial pressures are 0.05–0.15 bar. However, it appears to be more challenging to use conventional porous physisorbents for low-concentration CO_2 capture, as physisorbents tend to have low CO_2 uptake at low-concentrations (*i.e.* low partial pressures). The advantages of these physisorbents for CO_2 capture at low CO_2 concentrations fade significantly in terms of uptake capacity, selectivity, and adsorption kinetics. In the ideal case, a suitably engineered CO_2 sorbent for DAC would not only have high CO_2 uptake capacity at low CO_2 concentrations, but should also show high CO_2 selectivity under the relevant conditions. This means that the ΔH_{ads} of CO_2 sorption at zero or low loading must be significantly lower than that typically observed for physisorbents ($\sim$−20 to −40 kJ mol^{-1}). However, very low enthalpies of CO_2 sorption (*i.e.* <$\sim$−60 kJ mol^{-1}), or chemisorption of CO_2, may mean that regeneration of the sorbent will be energy-demanding.

Metal–organic frameworks (MOFs) are a type of porous coordination polymers constructed by linking metal ions or clusters with organic linkers *via* coordination bonds.[22,23] They usually have ordered porous channels and high specific surface areas. The rich coordination chemistry and large amount of available organic linkers endow MOFs with synthetic and structural diversity. Consequently, more than 90 000+ types of MOFs with defined structures have been synthesized so far.[24] The unique advantages of MOFs include tunable pore size and surface chemistry. The possibility to pre-design structures and composition renders MOFs attractive for many applications including low-concentration CO_2 capture.[25] For example, by judicious selection of the building units, the size, and shape of the pore-aperture of MOFs can be precisely tuned to achieve a high CO_2 separation efficiency by the molecular sieving effect.[26–28] Formation of ultramicropores,[29–31] creation of unsaturated metal centers,[32,33] and amine grafting[34,35] are effective approaches to introduce strong CO_2 adsorption sites on MOFs that can increase the binding affinity between the sorbents and CO_2. Such functionalized MOFs usually display high CO_2 uptake capacity and high selectivity, even at very low CO_2 concentrations. In this perspective, we will give an overview of the recent advances in the development and engineering of MOFs for low-concentration CO_2 capture. The relationship between the CO_2 capture performances (*e.g.* uptake capacity, selectivity, enthalpies of adsorption, kinetics, cyclic stability) and the MOF structures, as well as possible approaches to structure and upscale MOF sorbents for applications, will be discussed. We also discuss the prospects and challenges when it comes to the use of MOFs for CO_2 capture from low-concentration sources under different circumstances.

Strategies for enhancing CO_2 capture performance on MOFs

On MOFs, the general approach adopted to increase the CO_2 capture performance, especially for low-concentration CO_2 capture, is by tuning the sorption affinity for CO_2 at low-concentrations.[31] The CO_2 partial pressures (p_{CO_2}) that is of interest range from $\sim$0.4 to 10 mbar. This partial pressure range can be considered as equivalent to 400 ppm (current atmospheric CO_2 concentration) up to 10 000 ppm under atmospheric pressure, respectively. The CO_2 adsorption affinity at low-concentrations can be achieved through three main routes: (1) *via* careful control of the pore architecture of the frameworks, (2) through the introduction of high-energy sorption sites (*e.g.* open-metal sites, anionic groups), and (3) by post-synthetic amine-functionalization. In all cases, the CO_2 sorption isotherm of these MOFs should have a very sharp increase in the very low-pressure region (*i.e.* at 0.4 mbar for atmospheric CO_2 concentration). In this section, these three approaches will be discussed. The CO_2 capture performance of all the sorbents discussed in this paper are summarized in Table 1 for comparison.

Engineering pore architecture for CO_2 sorption

The typically weak CO_2 binding affinity on MOFs is related to physisorption-based processes. The weak interaction between CO_2 and the pore surface of MOFs is also indirectly linked to the low CO_2 selectivity over other gases, including the gaseous constituents of indoor air, such as O_2, N_2, and H_2O.[36] The development of MOF sorbents for low-concentration CO_2 capture through pore-size tailoring has been attained with a handful of materials. Ultramicroporous MOFs (*i.e.* frameworks containing pores with apertures <5–7 Å)[37] have remarkable CO_2 uptake capacities at low CO_2 concentrations due to their topological pore structures. The ultramicroporous MOF UTSA-16 is an example of such a structure with narrow pore apertures of 3.30 × 5.40 Å.[38] UTSA-16 was found to be capable of selectively interacting with CO_2 over other gases with a reported CO_2 uptake capacity of $\sim$0.95 mmol g^{-1} at p_{CO_2} = 50 mbar, 298 K.[39] The CO_2 molecules were found to interact with the terminal water molecules coordinated to K$^+$ ions, through hydrogen bonding, in the interior of the diamond-shaped cages (4.5 Å in diameter) in the framework. This interaction resulted in moderate ΔH_{ads} of CO_2 adsorption of $\sim$−39.7 kJ mol^{-1} (at near zero-coverage).[40] The hydrogen bonding interaction between the oxygen atoms in the CO_2 molecules and the crystallographically independent oxygen

Table 1 Comparison of the physical properties and CO_2 uptake capacities of various MOFs tested for low-concentration CO_2 capture. In studies where CO_2 uptake capacity is not list for very low pressures (*i.e.* <1 mbar), the CO_2 uptake capacity at ~50 mbar is listed

	CO_2 partial pressure (mbar)	Temperature (K)	Activation temperature (K)	Uptake (mmol g^{-1})	Uptake (cm^3 g^{-1})	ΔH_{ads} (kJ mol^{-1})	Ref.
NbOFFIVE-1-Ni	0.4	298	378	1.30	29.14	~−50 (1 mmol g^{-1} CO_2 loading)	44
SIFSIX-3-Ni	0.4	298	378	0.29	6.50	~−49.8 (1 mmol g^{-1} CO_2 loading)	44
ZU-36-Ni (GeFSIX-3-Ni)	0.4	298	373	1.07	23.98	~−55.5 (near-zero coverage)	45
ZU-36-Co (GeFSIX-3-Co)	0.4	298	373	0.30	6.72	~−39.1 (near-zero coverage)	45
SIFSIX-3-Cu	0.4	298	323	1.24	27.79	−54 (~0.25 mmol g^{-1} CO_2 loading)	46
TIFSIX-3-Ni	0.4	298	347/433	1.15[a]	25.78	~−53 (near-zero coverage)	31 and 47
NbOFFIVE-1-Ni	0.4	298	378	1.23[a]	27.57	~−54.9 (~0.1 mmol g^{-1} CO_2 loading)	47
SIFSIX-3-Cu-i	0.4	298	293	0.684	15.33	−32 (near-zero coverage)	46 and 48
SIFSIX-3-Zn	0.4	298	393	0.13	2.91	~−45 (near-zero coverage)	46 and 49
Mg-MOF-74	0.4	298	453	0.14[a]	3.14	~−41.5 (~0.1 mmol g^{-1} CO_2 loading)	47 and 50
Zn(ZnOH)$_4$(bibta)$_3$	0.4	300	373	2.20	49.31	~−42 (near-zero coverage) ~−71 (~2.0 mmol g^{-1} CO_2 loading)	51
Pyrazine-functionalized Co-MOF-74	0.4	298	393	1.36	30.48	−48.4 (near-zero coverage)	52
Co-MOF-74	0.4	298	393	0.65[a]	14.57	—	52
ZU-16-Co (TIFSIX-3-Co)	0.4	298	373	1.05	23.53	—	53
mmen-Mg$_2$(dobpdc)	0.4	298	343	2.00[a]	44.83	—	54
en-Mg$_2$(dobpdc)	0.4	298	343	2.50[a]	56.04	—	54
en-Mg$_2$(dobpdc)	0.39	298	403	2.83	63.43	~−22.5 (near-zero coverage) ~−49−−51 (~1.25−2.0 mmol g^{-1} CO_2 loading)	55
Mg$_2$(dobdc)(N$_2$H$_4$)$_{1.8}$	0.4	298	403	3.89	87.19	−90 (Virial) −118 (Clausius–Clapeyron)	56
SIFSIX-3-Ni	1	298	378	0.62	13.90	~−49.8 (1 mmol g^{-1} CO_2 loading)	44
SIFSIX-3-Cu	1	298	378	1.72	38.55	~−53 (~1.05 mmol g^{-1} CO_2 loading)	44
ZU-36-Ni (GeFSIX-3-Ni)	1	298	373	1.55	34.74	~−55.5 (near-zero coverage	45
ZU-36-Co (GeFSIX-3-Co)	1	298	373	0.75	16.81	~−39.1 (near-zero coverage)	45
SIFSIX-3-Cu	1	298	323	1.75	39.22	—	46
NbOFFIVE-1-Ni	1	298	378	1.68	37.66	—	44
TIFSIX-3-Ni	1	298	347/433	1.50[a]	33.62	~−53 (near-zero coverage)	31 and 47
Mg-MOF-74	1	298	453	0.33[a]	7.40	~−41.5 (~0.1 mmol g^{-1} CO_2 loading)	47
Zn(ZnOH)$_4$(bibta)$_3$	1	300	373	2.35[a]	52.67	~−42 (near-zero coverage) ~−71 (~2.0 mmol g^{-1} CO_2 loading)	51
Pyrazine-functionalized Co-MOF-74	1	298	393	2.10[a]	47.07	−48.4 (near-zero coverage)	52
Co-MOF-74	1	298	393	0.90[a]	20.17	—	52
ZU-16-Co (TIFSIX-3-Co)	1	298	373	1.55[a]	34.74	—	53
mmen-Mg$_2$(dobpdc)	1	298	343	3.00[a]	67.24	—	54
en-Mg$_2$(dobpdc)	1	298	343	3.20[a]	71.72	—	54
en-Mg$_2$(dobpdc)	1	298	403	3.10[a]	69.48	~−22.5 (near-zero coverage) ~−49−−51 (~0.13−2.0 mmol g^{-1} CO_2 loading)	55
Mg$_2$(dobdc)(N$_2$H$_4$)$_{1.8}$	1	298	403	4.35[a]	97.50	−90 (Virial) −118 (Clausius–Clapeyron)	56

Table 1 *(Contd.)*

	CO_2 partial pressure (mbar)	Temperature (K)	Activation temperature (K)	Uptake (mmol g^{-1})	Uptake (cm^3 g^{-1})	ΔH_{ads} (kJ mol^{-1})	Ref.
SIFSIX-3-Cu	40	298	323	2.36[a]	52.90	−54 (~0.25 mmol g^{-1} CO_2 loading)	46
SIFSIX-3-Zn	40	298	323	2.19[a]	49.09	~−45 (near-zero coverage)	46
UTSA-16	50	298	363	0.95[a]	21.29	−39.7 (near-zero coverage)	39 and 40
Zn$_2$(Atz)$_2$Ox (MeOH)	50	293	373/353	1.10[a]	24.66	−40.8 (near-zero coverage)	41 and 42
Zn$_2$(Atz)$_2$Ox (H$_2$O)	50	283	423	2.70[a]	60.52	~−55 (near-zero coverage)	43
JLU-MOF56	50	298	303	0.25[a]	5.60	~−30 (near-zero coverage)	57
JLU-MOF57	50	298	303	0.09[a]	2.02	~−32.5 (near-zero coverage)	57
Cu-F-pym	50	298	393	0.53[a]	11.88	~−30 (near-zero coverage)	58
UTSA-280	50	298	383	0.85[a]	19.05	−42.9 (near-zero coverage)	59
SIFSIX-3-Ni	50	293	413	2.45[a]	54.91	—	50
ZU-36-Ni (GeFSIX-3-Ni)	50	298	373	2.60[a]	58.28	~−55.5 (near-zero coverage	45
ZU-36-Co (GeFSIX-3-Co)	50	298	373	2.65[a]	59.40	~−39.1 (near-zero coverage)	45
Zn(ZnOH)$_4$(bibta)$_3$	50	300	373	3.00[a]	67.24	~−42 (near-zero coverage) ~−71 (~2.0 mmol g^{-1} CO_2 loading)	51
Pyrazine-functionalized Co-MOF-74	50	298	393	6.60[a]	147.93	−48.4 (near-zero coverage)	52
Co-MOF-74	50	298	393	5.20[a]	116.55	—	52
ZU-16-Co (TIFSIX-3-Co)	50	298	373	2.75[a]	61.64	—	53
mmen-Mg$_2$(dobpdc)	50	298	343	3.40[a]	76.21	—	54
en-Mg$_2$(dobpdc)	50	298	343	3.60[a]	80.69	—	54
en-Mg$_2$(dobpdc)	50	298	403	3.50[a]	78.45	~−22.5 (near-zero coverage) ~−49−−51 (~0.13–2.0 mmol g^{-1} CO_2 loading)	55
Mg$_2$(dobdc)(N$_2$H$_4$)$_{1.8}$	50	298	403	5.10[a]	114.31	−90 (Virial method) −118 (Clausius–Clapeyron)	56
SIFSIX-3-Ni	Lab atmosphere, 49% RH	296.55	413	0.18[a]	4.03	—	50
MIL-101(Cr)	10 vol% CO_2 (0.1 atm) 100 ppm SO$_2$, 100 ppm NO, 10% RH	298	473	0.48	10.78	—	60

[a] Data extracted from the original publication, and may be approximate.

atoms in H$_2$O was also found to account for 74% of the total CO_2 uptake capacity.[38] Similarly, Vaidhyanathan *et al.*[41,42] and Banerjee *et al.*[43] reported on a series of solvothermally synthesized ultramicroporous zinc-based aminotriazolate/ oxalate (Atz/Ox) MOFs (Zn$_2$(Atz)$_2$Ox (solvent)). Specifically, Zn$_2$(Atz)$_2$Ox (MeOH) was observed to possess pore channels with apertures of 3.50 × 4.00 Å along the *a*-axis, 3.90 × 2.10 Å along the *b*-axis, and narrow slit-shaped pores (3.00 × 1.60 Å) along the *c*-axis, respectively. The primary amino-groups on the aminotriazolate ligands were found to protrude into the cube-shaped pore cavities (4.00 × 4.00 × 4.00 Å) along the *a*-axis. The high CO_2 uptake capacity of the framework (~1.1 mmol g^{-1} at p_{CO_2} = 50 mbar, 293 K) was found to be due to both pore-size effects as well as from CO_2–amine inter- actions. This was also indicated by the relatively low ΔH_{ads} of CO_2, ~−40.8 kJ mol^{-1} at near zero-coverage.[41,42] Similarly, Zn$_2$(Atz)$_2$Ox (H$_2$O) was shown to possess the same oxalate-pil- lared structure as Zn$_2$(Atz)$_2$Ox (MeOH) with comparable pore

channels and apertures − 5.35 × 5.35 Å along the *a*-axis, 6.40 × 6.40 Å along the *b*-axis, and 5.80 × 5.25 Å along the [0 1 1] direction, respectively (Fig. 1a).[43] However, unlike Zn$_2$(Atz)$_2$Ox (MeOH), the water-solvated Zn$_2$(Atz)$_2$Ox (H$_2$O) framework was observed to undergo a subtle CO_2-induced structural rearrangement at p_{CO_2} = 200 mbar, 273 K (Fig. 1b). This gate- opening effect was observed alongside the appearance of new adsorption sites (denoted as site I and site II) in the frame- work, which could be separated by their ΔH_{ads}. The ΔH_{ads} pre- gate opening (*i.e.* corresponding to site I) was shown to increase from −46 kJ mol^{-1} to −32 kJ mol^{-1} post-gate opening, where CO_2 adsorption occurred on site II. The ΔH_{ads} for the two sites mainly corresponded to amine–CO_2 (site I) and CO_2– CO_2 (site II) interactions.[43]

Liu *et al.* also reported on two isomorphic triazolate-based ultramicroporous MOFs, namely, JLU-MOF56 ([Ni$_2$(μ$_2$-Cl) (BTBA)$_2$·DMF]·Cl·3DMF) and JLU-MOF57 ([Co$_2$(μ$_2$-Cl) (BTBA)$_2$·DMF]·Cl·3DMF, where BTBA^{4-} = 3,5-bis(triazol-1-yl)

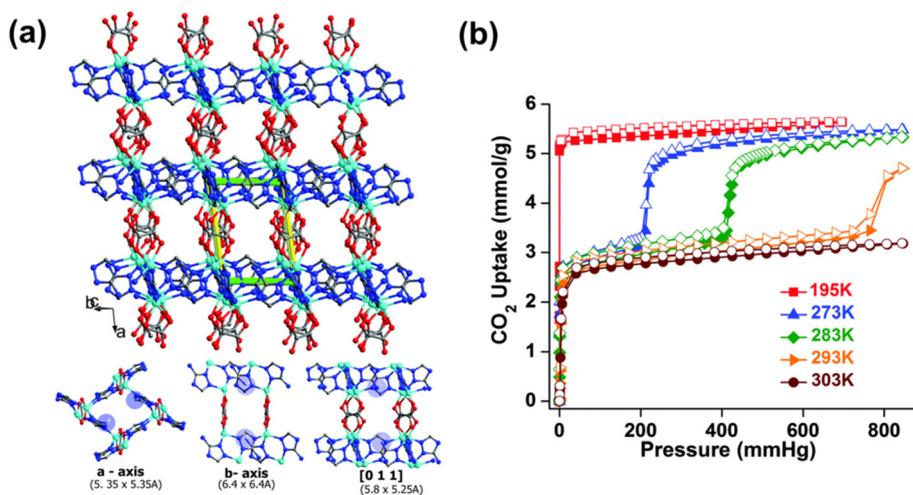**Fig. 1** (a) Three-dimensional structure of $Zn_2(Atz)_2Ox$ showing the ultramicroporous channels along a-, b- and c-axis, and (b) CO_2 sorption isotherms of $Zn_2(Atz)_2Ox$ at different temperatures.[43] Reproduced with permission, Copyright 2015 Royal Society of Chemistry.

benzoate, DMF = N,N'-dimethylformamide).[57] Both JLU-MOF56 and -57 featured channels with dimensions of 3.50 × 3.40 Å, 8.50 × 2.80 Å, and 3.50 × 3.40 Å along the a-, b-, and c-axis as well as internal cages 14 Å in diameter. Despite the presence of uncoordinated N-atom sites, the CO_2 uptake capacities of JLU-MOF56 (0.25 mmol g^{-1} at p_{CO_2} = 50 mbar, 298 K) and JLU-MOF57 (0.09 mmol g^{-1} at p_{CO_2} = 50 mbar, 298 K) were relatively low at low CO_2 concentrations. This was attributed to the significantly larger dimension of the cages in the framework as compared to the kinetic diameter of CO_2 (3.30 Å).[57] Navarro *et al.*[61] and Shi *et al.*[58] investigated the CO_2-sieving properties of an ultramicroporous MOF possessing appropriately sized channels as well as surface functionalities, namely, Cu-F-pym ($[Cu(F-pymo)_2(H_2O)_{1.25}]_n$, where F-pymo = 5-fluorpyrimidin-2-olate)). Cu-F-pym exhibited a 3D structure with **GIS**-related framework topology and possessed helical channels in the ab-plane with an aperture of 2.90 Å along the c-axis.[61] Selective adsorption of CO_2 (~0.53 mmol g^{-1} at p_{CO_2} = 53 mbar, 298 K) was observed on Cu-F-pym at ambient temperatures (*i.e.* 293 K) despite the narrow pore aperture. This was attributed to a thermal expansion of the Cu-F-pym framework which enabled the diffusion of CO_2 through the structure.[61] Pore-size tailoring has also been achieved using small non-functionalized linkers. An example of such was presented for the ultramicroporous MOF UTSA-280 ($[Ca(C_4O_4)(H_2O)] \cdot xH_2O$),[59,62] which utilizes squaric acid to form a 3D framework structure with cylindrical 1D channels (3.20 × 4.50 Å and 3.80 × 3.80 Å apertures) along the c-axis. The adsorbed CO_2 molecules were found, according to grand canonical Monte Carlo (GCMC) simulations, to interact with the organic linker as well as the coordinating water molecules in the pore channels through van der Waals and electrostatic interactions, giving rise to a ΔH_{ads} of CO_2 of ~-42.9 kJ mol^{-1} from the combined host–guest interactions.[59]

Hybrid ultramicroporous materials (HUMs) have garnered great attention in the last decade due to their unique structural properties. It is important to note that HUMs may not strictly be classified as MOFs, nevertheless, they will be included in this discussion for comparison. The prototypical HUM structure can broadly be described as 2D square **sql** nets composed of metal–organic units interconnected by pillaring inorganic anions (*e.g.* $[SiF_6]^{2-}$, $[TiF_6]^{2-}$, $[NbOF_5]^{2-}$, and $[GeF_6]^{2-}$, see Fig. 2).[45,47,63,64] The inherent structure of HUMs provides them with narrow and highly ordered pore channels that are decorated with polarizing atoms.[47,64] A comparison between the HUM SIFSIX-3-Ni and TEPA-SBA-15 (tetraethylenepentamine-functionalized mesoporous silica SBA-15) as well as Zeolite-13X was made by Kumar *et al.*[31,50] The authors showed that SIFSIX-3-Ni had superior CO_2 uptake capacity (0.18 mmol g^{-1}) as compared to Zeolite13X (0.03 mmol g^{-1}) at 1 bar pure CO_2 with 49% RH (296.55 K). However, the performance of the HUM was observed to be worse than TEPA-SBA-15 (3.59 mmol g^{-1}) under the same conditions. On TEPA-SBA-15, chemisorption of CO_2 accounted for its high CO_2 uptake, especially in the presence of water.[50] Fine-tuning of the CO_2 uptake properties in SIFSIX-3-M was further attained through the incorporation of different metal cations into the metal–organic unit of the structure. Bhatt *et al.*[44] observed a narrowing of the square channels in SIFSIX-3-Cu ($d_{F\cdots F}$ = 6.483(1) Å) when compared with SIFSIX-3-Ni ($d_{F\cdots F}$ = 6.694(1) Å) and SIFSIX-3-Zn ($d_{F\cdots F}$ = 6.784(1) Å), due to a reduced distance between adjacent $[SiF_6]^{2-}$ units. The narrowing of the channel resulted in an enhanced adsorbate–adsorbent interaction at low CO_2 concentrations. This enhanced interaction was also indicated by a decrease in the ΔH_{ads} from -45 kJ mol^{-1} on SIFSIX-3-Ni to -54 kJ mol^{-1} on SIFSIX-3-Cu. As further reported by Bhatt *et al.* the substitution of the pillaring anion from $[SiF_6]^{2-}$ to $[NbOF_5]^{2-}$ was also found to decrease the distance between the pendant fluorine moieties due to an increase in the bonding distance for Nb–F (d_{Nb-F} = 1.899(1) Å) as compared to Si–F (d_{Si-F} = 1.681(1) Å). An increase in volumetric CO_2 uptake at p_{CO_2} = 0.4 mbar by 15 to 340% was subsequently observed for
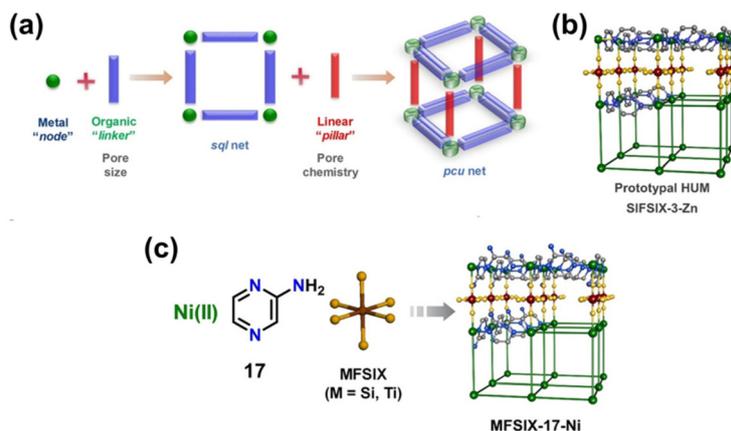
Fig. 2 (a) Schematic illustration of the modularity of pillared square grids that form the **pcu** topology of HUMs, (b) the prototypal pyrazine (pyz) linked HUM $[Zn(pyz)_2(SiF_6)]_n$, and (c) schematic illustration of the building blocks.[64] Reproduced with permission, Copyright 2021 John Wiley & Sons, Inc.

NbOFFIVE-1-Ni (1.3 mmol g^{-1} at 298 K) over SIFSIX-3-Cu (~1.25 mmol g^{-1} at 298 K), SIFSIX-3-Ni (~0.39 mmol g^{-1} at 298 K), and SIFSIX-3-Zn (~0.14 mmol g^{-1} at 298 K). The increase in CO$_2$ uptake was attributed to a further decrease in distance between pendant F···F moieties in NbOFFIVE-1-Ni ($d_{F\cdots F}$ = 3.210(8) Å) compared with SIFSIX-3-Cu ($d_{F\cdots F}$ = 3.483(1) Å) and SIFSIX-3-Ni ($d_{F\cdots F}$ = 3.694(1) Å).

Zhang *et al.*[45] reported the use of $[GeF_6]^{2-}$ units to slightly reduce the M–F distance (d_{Ge-F} = 1.83 Å) in the inorganic anions in ZU-36-Ni as compared to NbOFFIVE-1-Ni. The formation of an isostructural Co-based HUM, ZU-36-Co, was additionally investigated to assess the pore size and CO$_2$ uptake capacities in these ZU-36 frameworks. A shortening of the bond distance between the metal cation and the pyrazine linker in the square lattice of ZU-36-Co ($d_{Ni-pyrazine}$ = 2.12 Å) was achieved in ZU-36-Ni ($d_{Ni-pyrazine}$ = 2.08 Å). The decreased metal cation – pyrazine distance led to an enhanced CO$_2$ uptake capacity in the low-pressure range for ZU-36-Ni (1.07 mmol g^{-1} at p_{CO_2} = 0.4 mbar, 1.55 mmol g^{-1} at p_{CO_2} = 1 mbar CO$_2$, 298 K) and corresponded to an over 200% increase from ZU-36-Co (0.30 mmol g^{-1} at p_{CO_2} = 0.4 mbar, 0.75 mmol g^{-1} at p_{CO_2} = 1 mbar CO$_2$, 298 K). The CO$_2$ uptake capacity of ZU-36-Ni was found to be slightly lower than other HUMs such as SIFSIX-3-Cu (1.24 mmol g^{-1} at p_{CO_2} = 0.4 mbar, 1.75 mmol g^{-1} at p_{CO_2} = 1 mbar CO$_2$, 298 K) and NbOFFIVE-1-Ni (1.30 mmol g^{-1} at p_{CO_2} = 0.4 mbar, 1.68 mmol g^{-1} at p_{CO_2} = 1 mbar CO$_2$, 298 K). The difference in CO$_2$ uptake may be related to the more optimal F···F distances in SIFSIX-3-Cu and NbOFFIVE-1-Ni than in ZU-36.[45] Similarly, Kumar *et al.*[47] investigated another HUM structure that was isoreticular with SIFSIX-3-M, namely TIFSIX-3-Ni. The authors utilized $[TiF_6]^{2-}$ anionic pillars to further tailor the sorption properties of the SIFSIX-3-M framework. The M–F bond distance in TIFSIX-3-Ni (d_{Ti-F} = 1.81 Å) was found to be similar to Zu-36-Ni (d_{Ge-F} = 1.83 Å) and NbOFFIVE-1-Ni (d_{Nb-F} = 1.899(1) Å). The corresponding CO$_2$ uptake capacity at p_{CO_2} = 0.4 mbar of TIFSIX-3-Ni (~1.15 mmol g^{-1} at 298 K) was not found to differ significantly from NbOFFIVE-1-Ni (~1.23 mmol g^{-1} at 298 K) or ZU-36-Ni

(1.07 mmol g^{-1} at 298 K).[45] The presence of tight CO$_2$ binding sites was also observed in this framework, as indicated by a low ΔH_{ads} which was compared to other HUMs – TIFSIX-3-Ni, ~−49 kJ mol^{-1} (at 0.1 mmol g^{-1} CO$_2$ loading), NbOFFIVE-1-Ni, ~−54.9 kJ mol^{-1} (0.1 mmol g^{-1} CO$_2$ loading), ZU-36-Ni, −55.5 kJ mol^{-1} (at near-zero loading),[45] SIFSIX-3-Cu, ~−53.0 kJ mol^{-1} (0.1 mmol g^{-1} CO$_2$ loading).[44,50]

The impact of increasing the length of the organic molecule in the metal–organic unit in SIFSIX-3-Cu was further investigated by Shekhah *et al.*[46] through the substitution of pyrazine in SIFSIX-3-Cu by dipyridylacetylene. This approach resulted in the formation of the isoreticular HUM SIFSIX-2-Cu-i. The authors reported a decrease in CO$_2$ uptake capacity at p_{CO_2} = 0.4 mbar for SIFSIX-2-Cu-i (0.07 mmol g^{-1} at 298 K) when compared to SIFSIX-3-Cu (1.24 mmol g^{-1} at 298 K) and SIFSIX-3-Zn (0.13 mmol g^{-1} at 298 K). The decrease in CO$_2$ uptake was attributed to an increase in pore size from 3.5 Å in SIFSIX-3-Cu to 5.15 Å in SIFSIX-2-Cu-i. This enlargement of the average distance between the CO$_2$ molecules and the fluorine atoms in the channels of SIFSIX-2-Cu-i further led to a significantly increased ΔH_{ads} for CO$_2$ of ~−32 kJ mol^{-1} as compared to SIFSIX-3-Cu (−54 kJ mol^{-1}).[46] It is therefore clear that the ΔH_{ads} in MOF sorbents play a crucial role in their performance to capture CO$_2$. Many sorbents generally exhibit relatively low enthalpies of adsorption (<−50 kJ mol^{-1}) in the absence of ultramicropores or active functional groups. Thus leading to their poor performance at adsorbing CO$_2$ at low-concentrations. Various routes for improving the affinity between CO$_2$ molecules and a framework has been presented in the previous section, however, a compromise is generally required in order for these materials to be utilized in real-world applications. TSA processes were proposed by Lively *et al.*[65] to be more thermodynamically efficient as compared to PSA processes when utilizing sorbents with lower enthalpies of adsorption (*i.e.* <−50 kJ mol^{-1}) for dilute steams containing ~100–1000 ppm CO$_2$. The PSA process, on the other hand, was found to have low efficiency even for sorbents with relatively low CO$_2$ affinity (*i.e.* ΔH_{ads} >−35 kJ mol^{-1}). Although sorbents

with low enthalpies of CO_2 adsorption were found to be more suitable for trace CO_2 capture in TSA processes, it is important to note that a too low ΔH_{ads} will significantly increase the regeneration costs.

CO_2 sorption on high-energy sorption sites

Coordinatively unsaturated or open metal sites in MOFs have additionally been used to tune the CO_2 uptake capacity at low CO_2 concentrations. Strong interactions between such sites which exhibit electrostatic fields enable them to interact with the π-orbitals of polarizable guest molecules such as CO_2. The interaction between CO_2 and these high-energy adsorption sites is pivotal for low-concentration CO_2 capture.[66,67] Notably, MOFs such as M-MOF-74 (e.g. M = Mg^{2+}, Fe^{2+}, Co^{2+}, Zn^{2+}, Ni^{2+}), HKUST-1, and MIL-101 have been proposed for CO_2 capture at low CO_2 concentrations. Liu et al.[60] investigated the CO_2 capture performance of MIL-101(Cr), a mesoporous MOF containing Cr(III) with open metal sites. This MOF was observed to have a CO_2 uptake of 0.48 mmol g^{-1} at 298 K and 10% RH from a gas stream containing 100 000 ppm (~p_{CO_2} = 0.1 bar) CO_2 as well as 100 ppm SO_2, 100 ppm NO.[60] Kumar et al.[47] investigated the sorption properties of Mg-MOF-74 and HKUST-1 and compared them with TIFSIX-3-Ni and NbOFFIVE-1-Ni. At p_{CO_2} = 0.4 and 1 mbar, the CO_2 uptake capacities of Mg-MOF-74 (0.14 mmol g^{-1} at 0.4 mbar, 0.33 mmol g^{-1} at 1 mbar, 298 K) and HKUST-1 (no uptake at 0.4 mbar, 0.13 mmol g^{-1} at 1 mbar, 298 K) were significantly lower as compared to the HUMs. The ΔH_{ads} for Mg-MOF-74 (~-41.5 kJ mol^{-1} at 0.1 mmol g^{-1} CO_2 loading) and HKUST-1 (~-23 kJ mol^{-1} at 0.1 mmol g^{-1} CO_2 loading) further confirmed that the presence of open-metal sites in these frameworks can create strong binding sites for CO_2 as compared to conventional physisorption-based interactions. On the other hand, the narrow pore structure of HUMs,[44,47,64] such as those found in NbOFFIVE-1-Ni,[44] still offers higher energy CO_2 sorption sites (ΔH_{ads} ~-54.9 kJ mol^{-1}) than the open-metal sites on some MOFs.

Post-synthetic modification of MOFs for CO_2 capture

The introduction of functional groups, commonly through post-synthetic modifications, offers several advantages for increasing the binding interaction with CO_2. Typical functional groups include basic groups such as primary and secondary amines, polarizing halogen atoms, and larger hydrocarbon chains. Not only can these functional groups facilitate Lewis acid–base reactions (i.e. chemisorption-based adsorption processes), they can also increase the presence of strong electrostatic interactions, and possibly introduce steric effects to enhance adsorbate–adsorbent van der Waals interactions. As such, numerous studies on functionalized MOFs for trace CO_2 capture have been carried out. For example, Bien et al.[51] utilized a mild ligand exchange procedure to introduce nucleophilic sites in [Zn(ZnO$_2$CCH$_3$)$_4$(bibta)$_3$] (bibta^{2-} = 5,5′-bibenzotriazolate) to produce [Zn(ZnOH)$_4$(bibta)$_3$], as presented in the schematics shown in Fig. 3.[51] The post-synthetic modification resulted in significantly enhanced CO_2 uptake. The CO_2
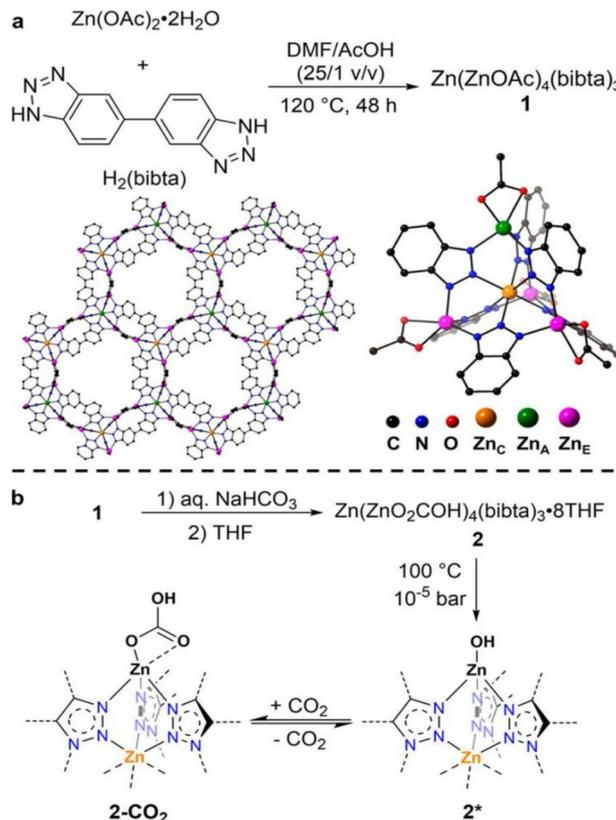

Fig. 3 (a) Synthesis structure of the Zn(ZnOAc)$_4$ SBUs. (b) Synthesis of Zn(ZnOH)$_4$(bibta)$_3$ and mechanism of reversible CO_2 fixation.[51] Reproduced with permission, Copyright 2013 American Chemical Society.

uptake capacity of the modified [Zn(ZnOH)$_4$(bibta)$_3$] was 2.20 mmol g^{-1} (0.4 mbar, 300 K), which was a significant improvement as compared to the negligible uptake on [Zn(ZnO$_2$CCH$_3$)$_4$(bibta)$_3$] under the same conditions. The chemisorption of CO_2 in [Zn(ZnOH)$_4$(bibta)$_3$] was further confirmed by the low ΔH_{ads} for the MOF (-71 kJ mol^{-1} at ~2.0 mmol g^{-1} CO_2 loading) thus indicating that CO_2 fixation likely occurred via a reversible Zn-OH/Zn–O(COOH) route (Fig. 3).[51] Hu et al.[52] also successfully obtained a pyrazine-functionalized Co-MOF-74 by post-synthesis modification. The effective pore size of the Co-MOF-74 was reduced from 11–12 Å down to <7 Å,[68] at the same time, Lewis basic sites were introduced from the non-coordination N-atoms on the pyrazine molecules. CO_2 uptake for the pyrazine-functionalized Co-MOF reached 1.26 mmol g^{-1} (0.4 mbar at 298 K), which was significantly higher than its non-functionalized counterpart (~0.65 mmol g^{-1} at 0.4 mbar and 298 K). The uptake capacity on the functionalized MOF was however slightly lower as compared to other high-performing MOFs such as TIFSIX-3-Ni (~1.1 mmol g^{-1} at 298 K)[31] and ZU-16-Co (~1.05 mmol g^{-1} at 298 K).[53] Correspondingly, the ΔH_{ads} of the pyrazine-functionalized Co-MOF-74 was higher (-48.4 kJ mol^{-1} at zero loading) than other frameworks with highly tailored pore structures (e.g. NbOFFIVE-1-Ni, -54.9 kJ mol^{-1} at 0.1 mmol g^{-1} CO_2

loading)[47] or chemisorption-based sorbents (*e.g.* [Zn (ZnOH)$_4$(bibta)$_3$], −71 kJ mol^{-1} at ~2.0 mmol g^{-1} CO$_2$ loading).[51,52] The moderate ΔH_{ads} of the functionalized MOF was however noticeably lower than the ΔH_{ads} of typical physisorbents, but not as low as the ΔH_{ads} of chemisorbents. This gives pyrazine-functionalized Co-MOF-74 an advantage over other sorbents with respect to energy costs for regeneration.

Similarly, MOFs with coordinatively unsaturated sites have commonly been used to post-synthetically introduce amine moieties. Lewis acid–base reactions between the CO$_2$ molecules and the accessible amine groups (*e.g.* primary or secondary amines) on the pore surfaces generally lead to the formation of carbamic acid followed by ammonium carbamate in the presence of humidity.[35,69] Notable examples include M-MOF-74, Mg$_2$(dobpdc) (dobpdc^{4-} = 4,4′-dioxido-3,3′-biphenyldicarboxylate), and MIL-101(Cr).[70] Park *et al.* grafted various diamines on to the pores of Mg$_2$(dobpdc) to increase the CO$_2$ binding affinity.[54] Linear and branched diamines with ethylene and propylene linkages were introduced post-synthetically onto Mg$_2$(dobpdc) (Fig. 4, 5a, and b). The CO$_2$ uptake capacity of N-isopropylethylenediamine-appended Mg$_2$(dobpdc) (mmen-Mg$_2$(dobpdc)) and ethylenediamine-appended MOFs at 400/1000 ppm were approximately 2.30/3.00 mmol g^{-1} and 2.50/3.20 mmol g^{-1}, respectively, at 298 K. The bulky N-isopropylethylenediamine introduced steric hindrance through the branched isopropyl-substituent, which may have kinetically restricted the CO$_2$ diffusion and the accessibility of the amine sites thus resulting in a slightly lower CO$_2$ uptake.[54] Similarly, Lee *et al.*[55] observed that the CO$_2$ uptake of ethylenediamine-appended Mg$_2$(dobpdc) (en-Mg$_2$(dobpdc)) was 2.83 mmol g^{-1} at 0.39 mbar, 298 K, which was 1.4 times higher than the N-isopropylethylenediamine-functionalized counterpart of the MOF (mmen-Mg$_2$(dobpdc) at 2.00 mmol g^{-1} (0.39 mbar, 298 K). The higher uptake capacity of en-Mg$_2$(dobpdc) as compared to mmen-Mg$_2$(dobpdc) at low CO$_2$ pressures was hypothesized by Lee *et al.*[55] and McDonald *et al.*[34] to be related to two factors: (1) the higher accessibility of the primary amine moieties in en-Mg$_2$(dobpdc), and (2) due to a large increase in entropy connected with the reorganiz-
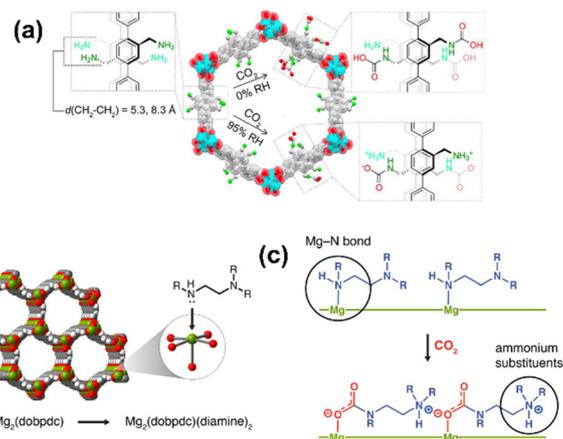

Fig. 5 (a) Chemisorption species post-CO$_2$ adsorption in IRMOF-74-III-(CH$_2$NH$_2$)$_2$.[35] (b) Representative structure of the metal–organic framework Mg$_2$(dobpdc). Green, red, gray, and white spheres represent Mg, O, C, and H atoms, respectively. (c) Depiction of cooperative CO$_2$ insertion into a row of Mg^{2+}–diamine sites to form ammonium carbamate chains along the pore axis.[88] Reproduced with permission, Copyright 2017 American Chemical Society.

ation of the secondary amines required for chemisorption of CO$_2$. These two factors led to preferential CO$_2$ adsorption onto low-energy sites (*i.e.* not associated with amine groups) and weak amine sites. The ΔH_{ads} between ~1.25–2.0 mmol g^{-1} CO$_2$ loading was estimated to range from −49 to −51 kJ mol^{-1} and corresponded well with the enthalpy of formation (ΔH_f) of carbamic acid (−52.8 kJ mol^{-1}). Additionally, a pressure-induced phase change was also observed in mmen-Mg$_2$(dobpdc), giving rise to a sharp increase in CO$_2$ uptake at ~0.2 mbar (298 K). This phenomenon was attributed to a cooperative CO$_2$ adsorption process wherein the deprotonation of the metal-bound amine by an adjacent non-coordinating amine moiety triggered a nucleophilic addition of CO$_2$. The resulting formation of a carbamate-ammonium ion pair in turn had a destabilizing effect on the metal-bound amine on the neighboring molecule. This destabilization, in turn, initiated the adsorption of
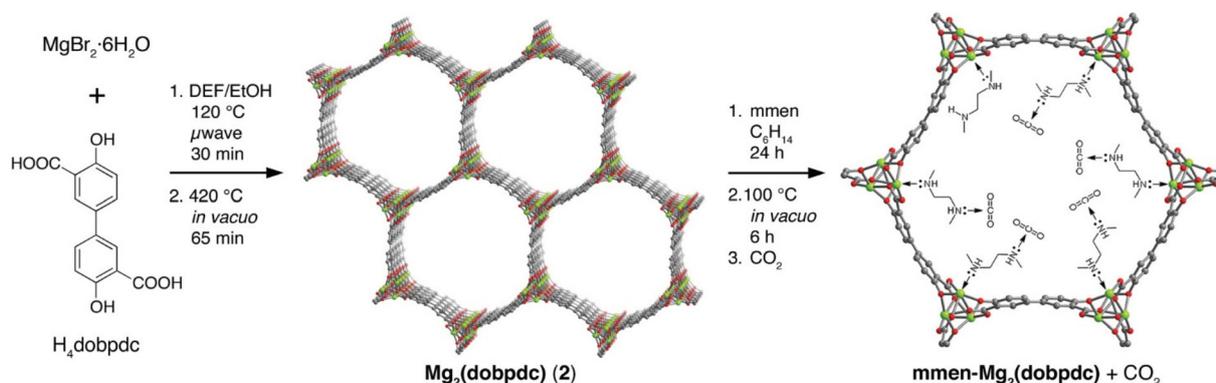

Fig. 4 (Left) Schematic of synthesis of Mg$_2$(dobpdc) and (middle) the amine-functionalization process to produce mmen-Mg$_2$(dobpdc), (right) interaction between pre-treated (degassed) mmen-Mg$_2$(dobpdc) and CO$_2$ molecules. Green, red, and gray spheres represent Mg, O, and C atoms respectively; H atoms are omitted for clarity.[34] Reproduced with permission, Copyright 2012 American Chemical Society.

another CO_2 molecule through the same process, as described in Fig. 5c.[71] Furthermore, adjacent non-coordinating amines were found to interact through hydrogen bonding in the absence of CO_2[72] which may prevent these groups from participating in the CO_2 adsorption process at pressures below ~0.2 mbar.[56,71]

Liao et al.[56] proposed that the incorporation of smaller diamine-species could increase the intermolecular distance between the uncoordinated amines and thus reduce the energetic favorability of hydrogen bonding between the moieties. An enhanced CO_2 uptake capacity in the hydrazine (N_2H_4)-functionalized Mg_2(2,5-dihydroxy-1,4-benzenedicarboxylate – dobdc), $[Mg_2(dobdc)(N_2H_4)_{1.8}]$ of 3.89 mmol g^{-1} at ~0.4 mbar (298 K) was observed. The CO_2 uptake of the $[Mg_2(dobdc)(N_2H_4)_{1.8}]$ was higher than mmen-Mg_2(dobpdc) (2.0 mmol g^{-1} ~0.4 mbar at 298 K)[55] as well as en-Mg_2(dobpdc) (2.85 mmol g^{-1} ~0.4 mbar at 298 K).[55] The low ΔH_{ads} (−118 kJ mol^{-1} at zero-coverage), in conjunction with observations from in-situ infrared spectroscopy, supported the formation of carbamate, which was found to be possible due to the long intramolecular distances between neighboring amines. An absence of proton-transfer during the adsorption process was also observed from the spectroscopic measurements.[56]

The three different approaches used to engineer MOFs for low-concentration CO_2 capture discussed here mainly aim to increase the interaction between CO_2 and the adsorption site. All three approaches have been shown to work effectively. The balance between having sufficiently low ΔH_{ads} of CO_2 to selectivity capture CO_2 at low-concentration, with low enough activation energy for sorption to take place at ambient temperature, and allowing desorption to take place with minimal energy input is perhaps the biggest challenge that deserves continued attention.

CO_2 selectivity, adsorption kinetics, and sorbent stability

As discussed, an ideal sorbent for CO_2 capture at low CO_2 concentrations should have strong binding interactions with CO_2, high CO_2 uptake capacities at low-concentrations, and relatively low ΔH_{ads} of CO_2. The utilization of MOFs as CO_2 sorbents in real-life applications is strongly dependent on (1) the selective adsorption of CO_2 over other gaseous constituents in air (particularly H_2O), (2) the framework stability in the presence of guest species, as well as (3) the ΔH_{ads} which plays a pivotal role in sorbent regeneration.

Various factors affect the gas selectivity of a sorbent, which include the topological structure and surface chemistry of the materials, and the physicochemical properties of the gas in question. The low CO_2 partial pressure at low CO_2 concentrations (i.e. <1 mbar), in conjunction with the significant presence of other gas molecules (e.g. H_2O, N_2, O_2 – physical properties of these gases are shown in Table 2) present a remarkably challenging problem for the selective capture of CO_2 in these conditions. Kinetic (also known as partial molecular sieve action) and thermodynamic effects likely play a crucial role in the overall observed CO_2 selectivity of a sorbent.[77] Shekhah et al. observed significantly stronger and more rapid

Table 2 Physical properties of gases commonly found in a mixture with CO_2 in low-concentration CO_2 capture-related application sources[73–76]

Gas molecule	Kinetic diameter (Å)	Polarizability (10^{-25} cm^3)	Dipole moment (10^{18} esu^{-1} cm^{-1})	Quadrupole moment (10^{26} esu^{-1} cm^{-2})
CO_2	3.30	29.1	0	4.30
H_2O	2.65	14.5	1.85	—
N_2	3.68	17.4	0	1.52
O_2	3.46	15.8	0	0.39

adsorption of CO_2 in SIFSIX-3-Cu than O_2, CH_4, and H_2. The strong and fast adsorption of CO_2 was attributed to a combined kinetic and thermodynamic effect. Partial sieving was achieved in the HUM due to the small size of the CO_2 molecules in conjunction with the large quadrupole moment and polarizability of CO_2. These factors combined enhanced the favorable interaction between CO_2 and the adsorption sites on the HUM.[46]

On the other hand, amine-modified MOFs rely heavily on the accessibility of the amine-sites on the pore surface as well as the formation of necessary intermediate species that govern the chemisorption process. The formation of carbamate/ammonium ion pairs in MOFs, such as that seen on mme-Mg_2(dobpdc) have been found to proceed through the formation of an intermediate species and subsequently followed by a transition state (Fig. 5 and in ref. 71). Although energy is required for the chemisorption process to take place, high temperatures will also simultaneously drive the reaction back towards the starting species, as the formation of the intermediate species is entropically unfavored. Thus, the formation rate of the product is limited by the intermediate species and the rate-limiting step in the reaction is attributed to the chemisorption process.[78] Stability of the frameworks in the presence of moisture presents an obstacle from a structural integrity point of view and can severely limit the applicability of MOFs in CO_2 capture, especially from humid gas mixtures with low CO_2 concentrations. The overall chemical and thermal stability of MOFs could be improved by utilizing high-valence metals (e.g. Zr^{4+} and Al^{3+}), which tend to form strong coordination bonds with carboxylate-based organic ligands, or similarly, lower-valence metals (i.e. soft metals such as Zn^{2+} and Cu^{2+}) which form strong coordination bonds with soft basic ligands. These approaches allow the formation of robust frameworks with enhanced stability that can cope with issues related to e.g. ligand displacement by water molecules.[79] Furthermore, the incorporation of ligands with hydrophobic functional groups (e.g. fluorine-containing,[80] alkyl-,[81] or ethyl ester-groups[82]) or groups that introduce steric effects[81,82] may impede the diffusion of water molecules through the framework and prevent hydrolysis. Therefore, careful consideration of the chemical compositions of the frameworks is necessary for the utilization of the MOFs in many real-world applications.

The susceptibility of amine species to thermal and oxidative degradation has also been well-documented in solution, *e.g.* in the case of monoethanolamine (MEA) which is commonly used in amine scrubbing for CO_2 capture and separation.[6,83–86] A handful of studies on amine-grafted solid sorbents, such as MCM-41 silica (TRI-PE-MCM-41), has shown primary amine to be more resilient towards oxidative degradation at high temperatures (>100 °C) as compared to secondary amines.[87] A cooperative degradation mechanism has also been suggested to take place in diamine-supported MCF silica involving the secondary and terminal primary amines.[88] However, the stability of amine-modified MOFs has, on the other hand, been studied to a lesser extent. Siegelman *et al.*[89] observed an improved oxidative stability of 2-ampd-Mg_2(dobpdc) (where 2-ampd = 2-(aminomethyl)piperidine) when exposed to a dry gas mixture (~21% O_2 and ~79% N_2 at 1 bar) at 100 °C for 5 h, as compared to many other silica-based materials functionalized with secondary amines. A negligible reduction in CO_2 uptake capacity was observed with the modified MOF as compared to the pristine material. Furthermore, no oxidative by-products of 2-ampd were detected by either ^1H NMR or IR spectroscopy, in contrast to amine-modified silicas that are prone to excessive oxidative degradation when treated in similar environments. The improved stability of 2-ampd-Mg_2(dobpdc) was attributed to the distance between the metal sites in the framework, which separates the amine species by ~7 Å in the pore channels, thus preventing oxidation reactions from taking place between adjacent amine moieties.[89] Furthermore, the incorporation of branched diamines (*e.g.* 1,1-dimethylethylenediamine and *N*-ethylethylenediamine) was found to improve the stability of functionalized Mg_2(dobpdc) as compared to primary diamines. Signifying that alkyl substituents may play a significant role in improving framework stability in the presence of oxygen and water vapor.[90,91]

Cost of sorbent production and scalability

Although MOFs show great potential in various application fields, several restrictions such as high synthesis cost, difficulties in scalability, and processability of MOFs need to be addressed before their commercialization and industrial applications can be achieved. In addition to the exploration of MOFs with new structures and applications, great efforts have been devoted to the development of cost-effective, green, and scalable approaches for the synthesis of MOFs. These approaches are especially important for candidate sorbents that are highly feasible for practical applications;[92–96] for example, M-MOF-74, UiO-66, HKUST-1, and MIL-series MOFs are relevant for trace CO_2 capture.

Metal ions and organic linkers are the two components for building a MOF structure. Metal nitrates and chlorides with high solubility and weak interfacial interactions are the most common metal sources for the synthesis of coordination complexes including MOFs.[92] However, the by-products containing chloride and nitrate ions are highly corrosive and toxic in general. Recent studies demonstrated that inexpensive metal acetates, hydroxides, and oxides can be used as precursors for low-impact synthesis of MOFs.[97] For example, MIL-53(Al)-NH_2 layers formed directly on the surface or in the channels of anodized aluminium oxide (AAO) substrates by solvothermal reactions, in which the aluminium oxides served as metal precursors to release aluminium ions for the construction of MOF structures.[98–100] The mixed-matrix membranes (MMMs) based on the AAO-MOF nanocomposites exhibited high CO_2/N_2 selectivities of 34–39 with extremely high CO_2 permeance of up to 3000 GPU (1 GPU = 3.35×10^{-10} mol cm^{-2} s^{-1} Pa^{-1}) that can potentially be developed for low-concentration CO_2 capture. In another example, Majano *et al.* demonstrated the conversion of $Cu(OH)_2$ into HKUST-1 at room temperature in an aqueous ethanoic solution with high space–time-yields (STY) up to 18 127 kg m^{-3} d^{-1}.[101] More importantly, the non-soluble nature of $Cu(OH)_2$ could avoid the release of copper ions into the solution that may ease the purification of the recycled solution. This synthesis approach opens new opportunities for the industrial production of HKUST-1 with low cost, low energy consumption, and minimal environmental impact. In addition, metal acetylacetonates (acac) with low toxicity are considered as green reagents in industrial processes that have been also used for the synthesis of various MOFs. Avci-Camur *et al.* synthesized several Zr(ɪv)-carboxylate based MOFs from Zr(acac)$_4$ with relatively high yields in water, including UiO-66-NH_2, UiO-66-$(OH)_2$, UiO-66-COOH, and UiO-66-$(COOH)_2$.[102]

Compared to the low cost and adequate availability of most metal precursors, the organic linkers involved in the synthesis of MOFs are usually costly. For example, polytopic carboxylic acids, the most common linkers for MOF synthesis, are prepared from petrochemical feedstocks through several steps involving the use of massive amounts of organic solvents and the generation of toxic by-products. Therefore, it is greatly desired to develop green MOF synthesis routes from renewable, affordable, and non-toxic linkers. Recently, several studies focused on the synthesis of bio-MOFs using biomolecules and biomass-derived organic compounds.[103] Biomolecules such as amino acids, nucleobases, proteins, peptides, cyclodextrins, tannins, and saccharides, which contain coordination sites of carboxylate groups or nitrogen and oxygen atoms with lone pairs of electrons have been successfully used for synthesizing a range of bio-MOFs.[104] Fumaric acid, a naturally available organic compound containing two carboxylic acid groups, has been constructed into several fumarate-based MOFs. For example, the aluminum fumarate MOF (Basolite A520), an analogue of MIL-53(Al), has been commercialized by BASF with high STYs of up to 5300 kg m^{-3} d^{-1} could be achieved.[105,106] Such bio-MOFs with good biocompatibility and low toxicity offer great hope for the development of many biological and medical applications.[107] In addition, several recent studies have investigated the potential of bio-MOFs for CO_2 capture.[108] Some of the bio-MOFs showed relatively high CO_2 capacity and selectivity at the conditions that are relevant to post-combustion capture of CO_2. For example, Basolite A520 with remarkable water stability and decent CO_2 uptake (2.1 mmol g^{-1} at 1 bar, 303 K) is suitable for CO_2 capture under wet conditions.[109] Bio-MOF-11, a cobalt-

adeninate obtained by the solvothermal reaction between cobalt acetate and adenine (a type of nucleobase), displayed a high CO_2 uptake of 6.0 mmol g^{-1} at 1 bar and 273 K and high calculated CO_2/N_2 selectivities up to 81 at 273 K.[110] However, the performance of bio-MOFs for low-concentration CO_2 capture is typically somewhat moderate when compared to the abovementioned top performing MOF-based CO_2 sorbents. We anticipate that future studies focusing on amine-modification of bio-MOFs will make these materials suitable for low-concentration CO_2 capture.

In addition to the metal sources and organic linkers, the selection of an appropriate solvent is vital for MOF synthesis, especially for the development of green and scalable synthesis approach. The physical properties of the solvent such as polarity, boiling point, viscosity, as well as the cost and environmental impact should be taken into consideration. DMF with a high boiling point and high polarity is widely employed for the synthesis of numerous MOFs under solvothermal conditions. However, the use of DMF not only increases the cost but also generates hazardous amines upon heating, which is not favourable for industrial-scale synthesis of MOFs. Remarkably, recent studies demonstrated that various MOFs including M-MOF-74, NH_2-MIL-53(Al), HKUST-1 can be synthesized in green solvents such as ethanol and water, and in some cases even at room temperature and ambient pressure.[96,111–115] For example, Huo et al. developed a facile, rapid, and industrially relevant approach for the synthesis of HKUST-1 in water at room temperature with high STY of >2000 kg m^{-3} d^{-1}. D'Amato et al. performed the reaction of cerium ammonium nitrate and tetrafluoroterephthalic acid in water and afforded a MOF with MIL-140 topology.[116] The obtained MOF exhibited an unusual S-shape CO_2 isotherm displaying a steep adsorption increase at pressure <0.03 bar at 273 K, which was an indication of the specific interactions of the quadrupolar CO_2 molecule (Table 2) with the MOF surface. The high CO_2 adsorption capacity at the low partial pressure, the exceptionally high CO_2/N_2 selectivity of up to 1900, as well as the green synthesis approach, shortlists this MIL-140 type MOF for possible application in low-concentration CO_2 capture. It is worth mentioning that MOFs with good CO_2 uptake capacity (2.5 mmol g^{-1} at 1 bar and 273 K) can be synthesized with bio-molecules in water at room temperature, as demonstrated by the synthesis of bismuth-based MOFs [Bi_2O $(H_2O)_2(C_{14}H_2O_8)\cdot nH_2O$], which was made using ellagic acid as the organic linker.[117] Still, solvent-based synthesis will inevitably produce liquid waste containing metal ions and organics that are harmful to the environment. The ideal case would be for the metal precursors and the organic linkers to be entirely converted into desired MOFs via solid-state reactions with no waste/by-products (including solvent waste). Mechanosynthesis has been shown as a green chemistry approach for the synthesis of a variety of functional porous materials such as covalent organic frameworks,[118] zeolites,[119] as well as MOFs.[120] For example, various MOFs have been successfully synthesized with high yields by ball mining or grinding of the starting materials at room temperature without any

solvent.[121] In some cases, trace-amount of solvent is needed to increase the reactivity of the reagent. The obtained MOFs have high specific surface areas and high crystallinity that are comparable to those prepared by conventional methods. For example, Julien et al. demonstrated the synthesis of highly porous and crystalline Zn-MOF-74 on a gram scale by mechanochemical milling of zinc oxide and 2,5-dihydroxyterephthalic acid without using bulk solvents. Their synthesis approach offers a fast, efficient, cost-effective, and environmentally friendly synthesis method in comparison with conventional solvothermal synthesis.[122] The milling reaction was monitored by real-time in-situ X-ray powder diffraction technique and it revealed a stepwise reaction mechanism. The formation of Zn-MOF-74 done by Julien et al. proceeds via a close-packed intermediate. Zhang et al. developed a solvent-free mechanochemical-assisted approach to the synthesis of ZU-36-Ni (GeFSIX-3-Ni).[45] Given the ultramicroporous structure, the obtained MOF displayed excellent performance for low-concentration CO_2 capture, exhibiting high CO_2 uptake of 1.07 mmol g^{-1} at 0.4 mbar and benchmark CO_2/N_2 separation selectivity of 4300 at 273 K. More interestingly, Chen et al. showed that mechanochemical methods can be applied in the synthesis of three-component MOFs consisting of mixed organic linkers. The method enables large-scale synthesis of ultramicroporous MOFs of Zn-atz-ipa and Zn-datz-ipa (atz = 3-amino-1,2,4-triazole, datz = 3,5-diamino-1,2,4-triazole, ipa = isophthalic acid) at room temperature with high STY up to 4800 kg m^{-3} d^{-1}.[123] Although not all studies discussed in this section have focused on low-concentration CO_2 capture, we believe that the different approaches could be applied to the development of MOFs targeted for low-concentration CO_2 capture.

Structuring of sorbents for real-life application

Prior to practical CO_2 capture applications, the as-synthesized MOFs sorbents have to be processed into certain shapes (e.g., pellets, granules, films, fibers). However, synthesis of MOFs typically yields solid crystalline powders that can be brittle, insoluble, and infusible. These features of the as-synthesized MOFs provide challenges in processing and shaping these sorbents and have significantly hampered their practical applications. The employment of conventional powder processing methods to shape MOF micro/nanocrystals, such as the use of binders, will block the porous channels and thus compromise the adsorption performances of the MOF sorbents.[124] For instance, Chang et al. developed a wet granulation method for shaping a family of MOF nano/microcrystals into mechanically strong granules with the assistance of 5 wt% of mesoporous RHO alumina as the inorganic binder. The shaping process involved wetting and mixing, granulation, and drying procedures, during which the interaction of hydroxyl groups on the MOF and the binder particles assisted in the formation of a monolithic structure. Similarly, Mathe et al. employed sucrose as an organic binder to process zirconium-based MOF powder into pellets via steps of mixing, sieving, and granulation. The MOF pellets can be produced on a kilogram scale in a relatively short operation time of 30 min. However, up to

50% of the porosity was lost during the shaping due to the pore-blocking effect.[125] Very recently, Lee *et al.* reported the scalable synthesis of highly uniform Mg-based MOF (Mg$_2$(dobpdc)) crystals along with the open-porous fiber networks for CO_2 capture.[126] Specifically, MgO particles were initially loaded into the porous poly(ether imide) (PEI) fiber matrix, and the obtained MgO/PEI precursor fiber was reacted with the organic linker by solvothermal treatment to convert the MgO particles into Mg$_2$(dobpdc) crystals. The Mg$_2$(dobpdc)/PEI composite was further soaked in diamine solution to form the fiber sorbents diamine-Mg$_2$(dobpdc)/PEI. Similarly, Quan *et al.* developed a straightforward and scalable approach to fabricate hollow fiber sorbents by incorporation of diamine-Mg$_2$(dobpdc) into poly(ethersulfone) (PES) substrate through a conventional "dry-jet, wet-quench" method.[127] These porous fiber sorbents showed unprecedented cyclic CO_2 capacities in conditions that are relevant to both post-combustion capture of CO_2 and low-concentration CO_2 capture. In addition, biopolymers such as cellulose, chitosan, have been recently studied as substrates to process MOFs into free-standing films and foams.[128–130] The use of such renewable and biodegradable substrates in MOF processing opens new possibilities to develop sustainable CO_2 sorbents based on MOF composites.

The emerging 3D printing technology, also known as additive manufacturing, could potentially overcome the drawbacks such as loss of surface area and clogging associated with applying conventional granulation and pelletization techniques in MOF processing.[131–134] The technique offers an opportunity to process MOFs into desired shapes and geometries in an easy-to-handle form. More importantly, the printed MOF composites could have high MOF loading with preserved MOF structure and properties. To date, various printing techniques including fused filament fabrication (FFF), digital light processing (DLP), selective laser sintering (SLS), and direct ink writing (DIW) have been employed to formulate MOFs for CO_2 adsorption and separation studies. Rezaei *et al.* employed DIW method to fabricate Ni-MOF-74 and UTSA-16(Co) powders into mechanically stable monoliths with the assistance of clay as a binder and poly(vinyl alcohol) (PVA) as a plasticizer.[135] The 3D-printed MOF monoliths had high MOF loading of up to 85 wt% and high surface areas of up to 737 m^2 g^{-1}. Remarkably, the CO_2 adsorption capacities of the MOFs were fully retained during the printing. The MOF monoliths showed relatively high CO_2 uptakes of >1.3 mmol g^{-1} at a low p_{CO_2} = 5 mbar and 298 K. In a similar approach, the same group prepared amine-functionalized MIL-101 monoliths, which showed high CO_2 uptakes of up to 1.6 mmol g^{-1} at p_{CO_2} = 3 mbar at 298 K.[136] It is noteworthy that the choices of solvent and binder are extremely important to form stable MOF monoliths *via* the DIW printing approach. Indeed, there are significant challenges for 3D printing MOFs at the industrial scale with concerns of cost and material stability. It is hoped that these issues will be addressed by future studies and 3D printing will be a powerful approach for processing various sorbents. We expected that the knowledge transfer from 3D printing to MOF processing would overcome the difficulties in shaping and structuring MOFs and promote their practical applications in trace CO_2 capture as well as various separation processes.

Conclusion and future outlook

Significant efforts in developing technologies to combat the high emission of CO_2 from point sources have been put in by researchers all over the world in the last few decades. CO_2 capture technologies have been implemented with the use of liquid-based amine scrubbing processes. In recent years, there has been notable development on adsorption-based technologies as an alternative to amine scrubbing. At the same time, low-concentration CO_2 capture, including direct air capture (DAC) and trace CO_2 capture (*i.e.* from very low partial pressures) through adsorption-based technologies have been put forward as the next step in reducing the atmospheric concentration of CO_2. However, for efficient low-concentration CO_2 capture, the ideal sorbent must be able to selectivity capture CO_2 with high CO_2 capacity. This means that the sorbent must have a high affinity for CO_2 (*i.e.* low enthalpy of CO_2 sorption), but not so high that the regeneration of the sorbent becomes energy intensive. A summary of the recent advances in the development of metal–organic frameworks (MOFs) and the closely related hybrid ultramicroporous materials (HUMs) was presented here. These potential sorbents have been engineered through different approaches to have many of the desirable properties needed for a good DAC CO_2 sorbent. Such approaches include pore size tuning, engineering open metal sites, and the introduction of functional groups with high affinities for CO_2 sorption. Significant advances have been made with respect to sorbent properties in recent years. Challenges remain in further improving the CO_2 uptake performance of these MOF sorbents, adopting sustainable, and energy-efficient green synthesis routes as well as structuring sorbents *via* innovative methods such as 3D printing.

Conflicts of interest

The authors declare that there are no conflicts of interest.

Acknowledgements

References

1 R. S. Haszeldine, *Science*, 2009, **325**, 1647–1652.

2 N. O. O. A. US, *Department of Commerce, Global Monitoring Laboratory – Carbon Cycle Greenhouse Gases, GML*, **https://gml.noaa.gov/ccgg/trends/gl_trend.html**, (accessed on December 5, 2022).

3 S. Mukherjee, A. Kumar and M. J. Zaworotko, in *Metal-Organic Frameworks (MOFs) for Environmental Applications*, ed. S. K. Ghosh, Elsevier, Amsterdam, 2019, ch. 2, pp. 5–61, DOI: **10.1016/B978-0-12-814633-0.00003-X.**

4 R. Custelcean, *Chem. Sci.*, 2021, **12**, 12518–12528.

5 T. Maldal and I. M. Tappel, *Energy*, 2004, **29**, 1403–1411.

6 G. T. Rochelle, *Science*, 2009, **325**, 1652–1654.

7 R. Ben-Mansour, M. A. Habib, O. E. Bamidele, M. Basha, N. A. A. Qasem, A. Peedikakkal, T. Laoui and M. Ali, *Appl. Energy*, 2016, **161**, 225–255.

8 N. Hedin, L. Andersson, L. Bergström and J. Yan, *Appl. Energy*, 2013, **104**, 418–433.

9 R. L. Siegelman, E. J. Kim and J. R. Long, *Nat. Mater.*, 2021, **20**, 1060–1072.

10 M. Sevilla and A. B. Fuertes, *Energy Environ. Sci.*, 2011, **4**, 1765–1771.

11 G. Singh, K. S. Lakhi, S. Sil, S. V. Bhosale, I. Kim, K. Albahily and A. Vinu, *Carbon*, 2019, **148**, 164–186.

12 C. Xu and M. Strømme, *Nanomaterials*, 2019, **9**, 103.

13 O. Cheung and N. Hedin, *RSC Adv.*, 2014, **4**, 14480–14494.

14 S. Kumar, R. Srivastava and J. Koh, *J. CO2 Util.*, 2020, **41**, 101251.

15 M. Xu, S. Chen, D.-K. Seo and S. Deng, *Chem. Eng. J.*, 2019, **371**, 693–705.

16 A. A. Dabbawala, I. Ismail, B. V. Vaithilingam, K. Polychronopoulou, G. Singaravel, S. Morin, M. Berthod and Y. Al Wahedi, *Microporous Mesoporous Mater.*, 2020, **303**, 110261.

17 W. Chaikittisilp, R. Khunsupat, T. T. Chen and C. W. Jones, *Ind. Eng. Chem. Res.*, 2011, **50**, 14203–14210.

18 C. Chen, S. Zhang, K. H. Row and W.-S. Ahn, *J. Energy Chem.*, 2017, **26**, 868–880.

19 W. Wang, M. Zhou and D. Yuan, *J. Mater. Chem. A*, 2017, **5**, 1334–1347.

20 L. Zou, Y. Sun, S. Che, X. Yang, X. Wang, M. Bosch, Q. Wang, H. Li, M. Smith, S. Yuan, Z. Perry and H.-C. Zhou, *Adv. Mater.*, 2017, **29**, 1700229.

21 C. Xu, G. Yu, J. Yuan, M. Strømme and N. Hedin, *Mater. Today Adv.*, 2020, **6**, 100052.

22 H. Furukawa, K. E. Cordova, M. O'Keeffe and O. M. Yaghi, *Science*, 2013, **341**, 1230444.

23 S. Kitagawa, R. Kitaura and S.-i. Noro, *Angew. Chem., Int. Ed.*, 2004, **43**, 2334–2375.

24 S. M. Moosavi, A. Nandy, K. M. Jablonka, D. Ongari, J. P. Janet, P. G. Boyd, Y. Lee, B. Smit, H. J. Kulik, S. M. Moosavi, A. Nandy, K. M. Jablonka, D. Ongari, J. P. Janet, P. G. Boyd, Y. Lee, B. Smit and H. J. Kulik, *Nat. Commun.*, 2020, **11**, 4068.

25 J. Liu, Y. Wei and Y. Zhao, *ACS Sustainable Chem. Eng.*, 2019, **7**, 82–93.

26 Q. Wang, J. Bai, Z. Lu, Y. Pan and X. You, *Chem. Commun.*, 2016, **52**, 443–452.

27 R.-B. Lin, Z. Zhang and B. Chen, *Acc. Chem. Res.*, 2021, **54**, 3362–3376.

28 M. Åhlén, A. Jaworski, M. Strømme and O. Cheung, *Chem. Eng. J.*, 2021, **422**, 130117.

29 Z. Zhang, S. B. Peh, R. Krishna, C. Kang, K. Chai, Y. Wang, D. Shi and D. Zhao, *Angew. Chem., Int. Ed.*, 2021, **60**, 17198–17204.

30 S. Nandi, P. De Luna, T. D. Daff, J. Rother, M. Liu, W. Buchanan, A. I. Hawari, T. K. Woo and R. Vaidhyanathan, *Sci. Adv.*, 2015, **11**, e1500421.

31 S. Mukherjee, N. Sikdar, D. O'Nolan, D. M. Franz, V. Gascón, A. Kumar, N. Kumar, H. S. Scott, D. G. Madden, P. E. Kruger, B. Space and M. J. Zaworotko, *Sci. Adv.*, 2019, **5**, eaax9171.

32 J. A. Mason, K. Sumida, Z. R. Herm, R. Krishna and J. R. Long, *Energy Environ. Sci.*, 2011, **4**, 3030–3040.

33 P. D. C. Dietzel, V. Besikiotis and R. Blom, *J. Mater. Chem.*, 2009, **19**, 7362–7370.

34 T. M. McDonald, W. R. Lee, J. A. Mason, B. M. Wiers, C. S. Hong and J. R. Long, *J. Am. Chem. Soc.*, 2012, **134**, 7056–7065.

35 R. W. Flaig, T. M. O. Popp, A. M. Fracaroli, E. A. Kapustin, M. J. Kalmutzki, R. M. Altamimi, F. Fathieh, J. A. Reimer and O. M. Yaghi, *J. Am. Chem. Soc.*, 2017, **139**, 12125–12128.

36 D. G. Madden, H. S. Scott, A. Kumar, K.-J. Chen, R. Sanii, A. Bajpai, M. Lusi, T. Curtin, J. J. Perry and M. J. Zaworotko, *Philos. Trans. R. Soc., A*, 2017, **375**, 20160025.

37 K. Adil, Y. Belmabkhout, R. S. Pillai, A. Cadiau, P. M. Bhatt, A. H. Assen, G. Maurin and M. Eddaoudi, *Chem. Soc. Rev.*, 2017, **46**, 3402–3430.

38 S. Xiang, Y. He, Z. Zhang, H. Wu, W. Zhou, R. Krishna and B. Chen, *Nat. Commun.*, 2012, **3**, 954.

39 A. Masala, F. Grifasi, C. Atzori, J. G. Vitillo, L. Mino, F. Bonino, M. R. Chierotti and S. Bordiga, *J. Phys. Chem. C*, 2016, **120**, 12068–12074.

40 A. Masala, J. G. Vitillo, F. Bonino, M. Manzoli, C. A. Grande and S. Bordiga, *Phys. Chem. Chem. Phys.*, 2016, **18**, 220–227.

41 R. Vaidhyanathan, S. S. Iremonger, K. W. Dawson and G. K. H. Shimizu, *Chem. Commun.*, 2009, 5230–5232.

42 R. Vaidhyanathan, S. S. Iremonger, G. K. H. Shimizu, P. G. Boyd, S. Alavi and T. K. Woo, *Science*, 2010, **330**, 650–653.

43 A. Banerjee, S. Nandi, P. Nasa and R. Vaidhyanathan, *Chem. Commun.*, 2016, **52**, 1851–1854.

44 P. M. Bhatt, Y. Belmabkhout, A. Cadiau, K. Adil, O. Shekhah, A. Shkurenko, L. J. Barbour and M. Eddaoudi, *J. Am. Chem. Soc.*, 2016, **138**, 9301–9307.

45 Z. Zhang, Q. Ding, S. B. Peh, D. Zhao, J. Cui, X. Cui and H. Xing, *Chem. Commun.*, 2020, **56**, 7726–7729.

46 O. Shekhah, Y. Belmabkhout, Z. Chen, V. Guillerm, A. Cairns, K. Adil and M. Eddaoudi, *Nat. Commun.*, 2014, **5**, 4228.

47 A. Kumar, C. Hua, D. G. Madden, D. O'Nolan, K.-J. Chen, L.-A. J. Keane, J. J. Perry and M. J. Zaworotko, *Chem. Commun.*, 2017, **53**, 5946–5949.

48 P. Nugent, Y. Belmabkhout, S. D. Burd, A. J. Cairns, R. Luebke, K. Forrest, T. Pham, S. Ma, B. Space, L. Wojtas, M. Eddaoudi and M. J. Zaworotko, *Nature*, 2013, **495**, 80–84.

49 K. Uemura, A. Maeda, T. K. Maji, P. Kanoo and H. Kita, *Eur. J. Inorg. Chem.*, 2009, 2329–2337.

50 A. Kumar, D. G. Madden, M. Lusi, K.-J. Chen, E. A. Daniels, T. Curtin, J. J. Perry IV and M. J. Zaworotko, *Angew. Chem., Int. Ed.*, 2015, **54**, 14372–14377.

51 C. E. Bien, K. K. Chen, S.-C. Chien, B. R. Reiner, L.-C. Lin, C. R. Wade and W. S. W. Ho, *J. Am. Chem. Soc.*, 2018, **140**, 12662–12666.

52 P. Hu, H. Liu, H. Wang, J. Zhou, Y. Wang and H. Ji, *J. Mater. Chem. A*, 2022, **10**, 881–890.

53 Z. Zhang, Q. Ding, J. Cui, X. Cui and H. Xing, *Sci. China Mater.*, 2020, **64**, 691–697.

54 J. Park, J. R. Park, J. H. Choe, S. Kim, M. Kang, D. W. Kang, J. Y. Kim, Y. W. Jeong and C. S. Hong, *ACS Appl. Mater. Interfaces*, 2020, **12**, 50534–50540.

55 W. R. Lee, S. Y. Hwang, D. W. Ryu, K. S. Lim, S. S. Han, D. Moon, J. Choi and C. S. Hong, *Energy Environ. Sci.*, 2014, **7**, 744–751.

56 P.-Q. Liao, X.-W. Chen, S.-Y. Liu, X.-Y. Li, Y.-T. Xu, M. Tang, Z. Rui, H. Ji, J.-P. Zhang and X.-M. Chen, *Chem. Sci.*, 2016, **7**, 6528–6533.

57 S. Liu, S. Yao, B. Liu, X. Sun, Y. Yuan, G. Li, L. Zhang and Y. Liu, *Dalton Trans.*, 2019, **48**, 1680–1685.

58 Y. Shi, Y. Xie, H. Cui, Z. A. Alothman, O. Alduhaish, R.-B. Lin and B. Chen, *Chem. Eng. J.*, 2022, **446**, 137101.

59 R.-B. Lin, L. Li, A. Alsalme and B. Chen, *Small Struct.*, 2020, **1**, 2000022.

60 Q. Liu, L. Ning, S. Zheng, M. Tao, Y. Shi and Y. He, *Sci. Rep.*, 2013, **3**, 2916.

61 J. A. R. Navarro, E. Barea, A. Rodríguez-Diéguez, J. M. Salas, C. O. Ania, J. B. Parra, N. Masciocchi, S. Galli and A. Sironi, *J. Am. Chem. Soc.*, 2008, **130**, 3978–3984.

62 R.-B. Lin, L. Li, H.-L. Zhou, H. Wu, C. He, S. Li, R. Krishna, J. Li, W. Zhou and B. Chen, *Nat. Mater.*, 2018, **17**, 1128–1133.

63 S. Subramanian and M. J. Zaworotko, *Angew. Chem., Int. Ed. Engl.*, 1995, **34**, 2127–2129.

64 S. Mukherjee, N. Kumar, A. A. Bezrukov, K. Tan, T. Pham, K. A. Forrest, K. A. Oyekan, O. T. Qazvini, D. G. Madden, B. Space and M. J. Zaworotko, *Angew. Chem., Int. Ed.*, 2021, **60**, 10902–10909.

65 R. P. Lively and M. J. Realff, *AIChE J.*, 2016, **62**, 3699–3705.

66 T. Quainoo, S. N. Lavan and Z.-F. Liu, *J. Mater. Res.*, 2021, **37**, 334–345.

67 Y. Xie, H. Cui, H. Wu, R.-B. Lin, W. Zhou and B. Chen, *Angew. Chem., Int. Ed.*, 2021, **60**, 9604–9609.

68 I. Strauss, A. Mundstock, M. Treger, K. Lange, S. Hwang, C. Chmelik, P. Rusch, N. C. Bigall, T. Pichler, H. Shiozawa and J. Caro, *ACS Appl. Mater. Interfaces*, 2019, **11**, 14175–14181.

69 A. C. Forse, P. J. Milner, J.-H. Lee, H. N. Redfearn, J. Oktawiec, R. L. Siegelman, J. D. Martell, B. Dinakar, L. B. Zasada, M. I. Gonzalez, J. B. Neaton, J. R. Long and J. A. Reimer, *J. Am. Chem. Soc.*, 2018, **140**, 18016–18031.

70 A. Sinha, L. A. Darunte, C. W. Jones, M. J. Realff and Y. Kawajiri, *Ind. Eng. Chem. Res.*, 2017, **56**, 750–764.

71 T. M. McDonald, J. A. Mason, X. Kong, E. D. Bloch, D. Gygi, A. Dani, V. Crocellà, F. Giordanino, S. O. Odoh, W. S. Drisdell, B. Vlaisavljevich, A. L. Dzubak, R. Poloni, S. K. Schnell, N. Planas, K. Lee, T. Pascal, L. F. Wan, D. Prendergast, J. B. Neaton, B. Smit, J. B. Kortright, L. Gagliardi, S. Bordiga, J. A. Reimer and J. R. Long, *Nature*, 2015, **519**, 303–308.

72 N. Planas, A. L. Dzubak, R. Poloni, L.-C. Lin, A. McManus, T. M. McDonald, J. B. Neaton, J. R. Long, B. Smit and L. Gagliardi, *J. Am. Chem. Soc.*, 2013, **135**, 7402–7405.

73 Y. A. Majid, S. K. Garg and D. W. Davidson, *Can. J. Chem.*, 1968, **46**, 1683–1690.

74 G. Sethia, R. S. Somani and H. C. Bajaj, *RSC Adv.*, 2015, **5**, 12773–12781.

75 X. Wang, L. Zhong, Y. Cressault, A. Gleizes and M. Rong, *J. Phys. D: Appl. Phys.*, 2014, **47**, 495201.

76 O. M. Yaghi, M. J. Kalmutzki and C. S. Diercks, in *Introduction to Reticular Chemistry: Metal-Organic Frameworks and Covalent Organic Frameworks*, ed. O. M. Yaghi, M. J. Kalmutzki and C. S. Diercks, Wiley-VCH Verlag GmbH & Co. KGaA, Weinheim, Germany, 2019, ch. 14, pp. 313–314, DOI: 10.1002/9783527821099.ch14.

77 J.-R. Li, R. J. Kuppler and H.-C. Zhou, *Chem. Soc. Rev.*, 2009, **38**, 1477–1504.

78 J. D. Martell, P. J. Milner, R. L. Siegelman and J. R. Long, *Chem. Sci.*, 2020, **11**, 6457–6471.

79 X. Zhang, B. Wang, A. Alsalme, S. Xiang, Z. Zhang and B. Chen, *Coord. Chem. Rev.*, 2020, **423**, 213507.

80 C. Yang, U. Kaipa, Q. Z. Mather, X. Wang, V. Nesterov, A. F. Venero and M. A. Omary, *J. Am. Chem. Soc.*, 2011, **133**, 18094–18097.

81 Y. Chen, B. Wang, X. Wang, L. H. Xie, J. Li, Y. Xie and J. R. Li, *ACS Appl. Mater. Interfaces*, 2017, **9**, 27027–27035.

82 J. M. Taylor, R. Vaidhyanathan, S. S. Iremonger and G. K. Shimizu, *J. Am. Chem. Soc.*, 2012, **134**, 14338–14340.

83 S. A. Bedell, C. M. Worley, K. Darst and K. Simmons, *Int. J. Greenhouse Gas Control*, 2011, **5**, 401–404.

84 K. Veltman, B. Singh and E. G. Hertwich, *Environ. Sci. Technol.*, 2010, **44**, 1496–1502.

85 K.-S. Zoannou, D. J. Sapsford and A. J. Griffiths, *Int. J. Greenhouse Gas Control*, 2013, **17**, 423–430.

86 H. Lepaumier, D. Picq and P.-L. Carrette, *Ind. Eng. Chem. Res.*, 2009, **48**, 9068–9075.

87 A. Heydari-Gorji, Y. Belmabkhout and A. Sayari, *Microporous Mesoporous Mater.*, 2011, **145**, 146–149.

88 P. Bollini, S. Choi, J. H. Drese and C. W. Jones, *Energy Fuels*, 2011, **25**, 2416–2425.

89 R. L. Siegelman, T. M. McDonald, M. I. Gonzalez, J. D. Martell, P. J. Milner, J. A. Mason, A. H. Berger, A. S. Bhown and J. R. Long, *J. Am. Chem. Soc.*, 2017, **139**, 10526–10538.

90 H. Jo, W. R. Lee, N. W. Kim, H. Jung, K. S. Lim, J. E. Kim, D. W. Kang, H. Lee, V. Hiremath, J. G. Seo, H. Jin, D. Moon, S. S. Han and C. S. Hong, *ChemSusChem*, 2017, **10**, 541–550.

91 W. R. Lee, J. E. Kim, S. J. Lee, M. Kang, D. W. Kang, H. Y. Lee, V. Hiremath, J. G. Seo, H. Jin, D. Moon, M. Cho, Y. Jung and C. S. Hong, *ChemSusChem*, 2018, **11**, 1694–1707.

92 S. Kumar, S. Jain, M. Nehra, N. Dilbaghi, G. Marrazza and K.-H. Kim, *Coord. Chem. Rev.*, 2020, **420**, 213407.

93 A. Garcia Marquez, P. Horcajada, D. Grosso, G. Férey, C. Serre, C. Sanchez and C. Boissiere, *Chem. Commun.*, 2013, **49**, 3848–3850.

94 T. He, X. Xu, B. Ni, H. Wang, Y. Long, W. Hu and X. Wang, *Nanoscale*, 2017, **9**, 19209–19215.

95 Y. Pan, Y. Liu, G. Zeng, L. Zhao and Z. Lai, *Chem. Commun.*, 2011, **47**, 2071–2073.

96 J. Huo, M. Brightwell, S. El Hankari, A. Garai and D. Bradshaw, *J. Mater. Chem. A*, 2013, **1**, 15220–15223.

97 G. Zhan and H. C. Zeng, *Chem. Commun.*, 2016, **53**, 72–81.

98 C. Yim, M. Lee, M. Yun, G.-H. Kim, K. T. Kim and S. Jeon, *Sci. Rep.*, 2015, **5**, 10674.

99 K. Xie, Q. Fu, C. Xu, H. Lu, Q. Zhao, R. Curtain, D. Gu, P. A. Webley and G. G. Qiao, *Energy Environ. Sci.*, 2018, **11**, 544–550.

100 Y. Yu, X.-J. Wu, M. Zhao, Q. Ma, J. Chen, B. Chen, M. Sindoro, J. Yang, S. Han, Q. Lu and H. Zhang, *Angew. Chem.*, 2017, **129**, 593–596.

101 G. Majano and J. Pérez-Ramírez, *Adv. Mater.*, 2013, **25**, 1052–1057.

102 C. Avci-Camur, J. Perez-Carvajal, I. Imaz and D. Maspoch, *ACS Sustainable Chem. Eng.*, 2018, **6**, 14554–14560.

103 I. Imaz, M. Rubio-Martínez, J. An, I. Solé-Font, N. L. Rosi and D. Maspoch, *Chem. Commun.*, 2011, **47**, 7287–7302.

104 S. L. Anderson and K. C. Stylianou, *Coord. Chem. Rev.*, 2017, **349**, 102–128.

105 E. Alvarez, N. Guillou, C. Martineau, B. Bueken, B. Van de Voorde, C. Le Guillouzer, P. Fabry, F. Nouar, F. Taulelle, D. de Vos, J.-S. Chang, K. H. Cho, N. Ramsahye, T. Devic, M. Daturi, G. Maurin and C. Serre, *Angew. Chem., Int. Ed.*, 2015, **54**, 3664–3668.

106 B. Yilmaz, N. Trukhan and U. Müller, *Chin. J. Catal.*, 2012, **33**, 3–10.

107 P. Horcajada, R. Gref, T. Baati, P. K. Allan, G. Maurin, P. Couvreur, G. Férey, R. E. Morris and C. Serre, *Chem. Rev.*, 2012, **112**, 1232–1268.

108 A. Zulys, F. Yulia, N. Muhadzib and N. Nasruddin, *Ind. Eng. Chem. Res.*, 2020, **60**, 37–51.

109 J. A. Coelho, A. M. Ribeiro, A. F. P. Ferreira, S. M. P. Lucena, A. E. Rodrigues and D. C. S. d. Azevedo, *Ind. Eng. Chem. Res.*, 2016, **55**, 2134–2143.

110 J. An, S. J. Geib and N. L. Rosi, *J. Am. Chem. Soc.*, 2010, **132**, 38–39.

111 M. Sánchez-Sánchez, N. Getachew, K. Díaz, M. Díaz-García, Y. Chebude and I. Díaz, *Green Chem.*, 2015, **17**, 1500–1509.

112 L. H. Wee, M. R. Lohe, N. Janssens, S. Kaskel and J. A. Martens, *J. Mater. Chem.*, 2012, **22**, 13742–13746.

113 J.-L. Zhuang, D. Ceglarek, S. Pethuraj and A. Terfort, *Adv. Funct. Mater.*, 2011, **21**, 1442–1447.

114 J. Shi, J. Zhang, D. Tan, X. Cheng, X. Tan, B. Zhang, B. Han, L. Liu, F. Zhang, M. Liu and J. Xiang, *ChemCatChem*, 2019, **11**, 2058–2062.

115 I. Pakamorè, J. Rousseau, C. Rousseau, E. Monflier and P. Á. Szilágyi, *Green Chem.*, 2018, **20**, 5292–5298.

116 R. D'Amato, A. Donnadio, M. Carta, C. Sangregorio, D. Tiana, R. Vivani, M. Taddei and F. Costantino, *ACS Sustainable Chem. Eng.*, 2019, **7**, 394–402.

117 E. S. Grape, J. G. Flores, T. Hidalgo, E. Martínez-Ahumada, A. Gutiérrez-Alejandre, A. Hautier, D. R. Williams, M. O'Keeffe, L. Öhrström, T. Willhammar, P. Horcajada, I. A. Ibarra and A. K. Inge, *J. Am. Chem. Soc.*, 2020, **142**, 16795–16804.

118 G. Das, D. B. Shinde, S. Kandambeth, B. P. Biswal and R. Banerjee, *Chem. Commun.*, 2014, **50**, 12615–12618.

119 D. N. Rainer and R. E. Morris, *Dalton Trans.*, 2021, **50**, 8995–9009.

120 A. M. Fidelli, B. Karadeniz, A. J. Howarth, I. Huskić, L. S. Germann, I. Halasz, M. Etter, S.-Y. Moon, R. E. Dinnebier, V. Stilinović, O. K. Farha, T. Friščić and K. Užarević, *Chem. Commun.*, 2018, **54**, 6999–7002.

121 S. Głowniak, B. Szczęśniak, J. Choma and M. Jaroniec, *Mater. Today*, 2021, **46**, 109–124.

122 P. A. Julien, K. Užarević, A. D. Katsenis, S. A. J. Kimber, T. Wang, O. K. Farha, Y. Zhang, J. Casaban, L. S. Germann, M. Etter, R. E. Dinnebier, S. L. James, I. Halasz and T. Friščić, *J. Am. Chem. Soc.*, 2016, **138**, 2929–2932.

123 T. Gao, H.-J. Tang, S.-Y. Zhang, J.-W. Cao, Y.-N. Wu, J. Chen, Y. Wang and K.-J. Chen, *J. Solid State Chem.*, 2021, **303**, 122547.

124 Z. Wang, L. Liu, Z. Li, N. Goyal, T. Du, J. He and G. K. Li, *Energy Fuels*, 2022, **36**, 2927–2944.

125 J. Ren, N. M. Musyoka, H. W. Langmi, A. Swartbooi, B. C. North and M. Mathe, *Int. J. Hydrogen Energy*, 2015, **40**, 4617–4622.

126 Y. H. Lee, Y. Kwon, C. Kim, Y.-E. Hwang, M. Choi, Y. Park, A. Jamal and D.-Y. Koh, *JACS Au*, 2021, **1**, 1198–1207.

127 W. Quan, H. E. Holmes, F. Zhang, B. L. Hamlett, M. G. Finn, C. W. Abney, M. T. Kapelewski, S. C. Weston, R. P. Lively and W. J. Koros, *JACS Au*, 2022, **2**, 1350–1358.

128 S. Sultan, H. N. Abdelhamid, X. Zou and A. P. Mathew, *Adv. Funct. Mater.*, 2019, **29**, 1805372.

129 S. Zhou, X. Kong, B. Zheng, F. Huo, M. Strømme and C. Xu, *ACS Nano*, 2019, **13**, 9578–9586.

130 X.-H. Ma, Z. Yang, Z.-K. Yao, Z.-L. Xu and C. Y. Tang, *J. Membr. Sci.*, 2017, **525**, 269–276.

131 E. R. Kearns, R. Gillespie and D. M. D'Alessandro, *J. Mater. Chem. A*, 2021, **9**, 27252–27270.

132 S. Lawson, X. Li, H. Thakkar, A. A. Rownaghi and F. Rezaei, *Chem. Rev.*, 2021, **121**, 6246–6291.

133 C. A. Grande, R. Blom, V. Middelkoop, D. Matras, A. Vamvakeros, S. D. M. Jacques, A. M. Beale, M. Di

Michiel, K. A. Andreassen and A. M. Bouzga, *Chem. Eng. J.*, 2020, **402**, 126166.

134 K. A. Evans, Z. C. Kennedy, B. W. Arey, J. F. Christ, H. T. Schaef, S. K. Nune and R. L. Erikson, *ACS Appl. Mater. Interfaces*, 2018, **10**, 15112–15121.

135 H. Thakkar, S. Eastman, Q. Al-Naddaf, A. A. Rownaghi and F. Rezaei, *ACS Appl. Mater. Interfaces*, 2017, **9**, 35908–35916.

136 S. Lawson, C. Griffin, K. Rapp, A. A. Rownaghi and F. Rezaei, *Energy Fuels*, 2019, **33**, 2399–2407.